Nano Energy 44 (2018) 272–278

Contents lists available at ScienceDirect

Nano Energy

journal homepage: www.elsevier.com/locate/nanoen

Full paper

$Li_3V(MoO_4)_3$ as a novel electrode material with good lithium storage properties and improved initial coulombic efficiency

Jiexi Wang[a,c,*,1], Guobin Zhang[b,1], Zhaomeng Liu[c,1], Hangkong Li[d], Yong Liu[a], Zhixing Wang[c], Xinhai Li[c], Kaimin Shih[d,**], Liqiang Mai[b,**]

[a] Powder Metallurgy Research Institute, Central South University, 932, Lushan South Road, Changsha 410083, PR China
[b] State Key Laboratory of Advanced Technology for Materials Synthesis and Processing, Wuhan University of Technology, Wuhan 430070, PR China
[c] School of Metallurgy and Environment, Central South University, 932, Lushan South Road, Changsha 410083, PR China
[d] Department of Civil Engineering, The University of Hong Kong, Hong Kong

ARTICLE INFO

Keywords:
$Li_3V(MoO_4)_3$
Pre-lithiation
Anode
Lithium storage
Initial coulombic efficiency

ABSTRACT

It is of great significance to discover new negative electrode materials featuring a low operating voltage, high capacity and improved initial coulombic efficiency for lithium ion batteries. This is the first report on the use of orthorhombic $Li_3V(MoO_4)_3$ as a promising anode material that exhibits natural advantages over reported traditional metal oxides. High-crystalline $Li_3V(MoO_4)_3$ nanoparticles decorated with carbon are synthesized by a facile mechanochemical route followed by low-temperature (480 °C) calcination. The lithium storage ability of the prepared $Li_3V(MoO_4)_3$ anode is fully tapped at 3.0–0.01 V vs. Li^+/Li, displaying a lower voltage plateau than the conversion-type metal oxides. It delivers a high reversible specific capacity of 999 mAh g^{-1} at 50 mA g^{-1} and a high coulombic efficiency of 82.6%. Moreover, it maintains a capacity retention of 92% after 75 cycles at 500 mA g^{-1}. The GITT-determined Li^+ diffusion coefficient ranges from 10^{-10} to 10^{-13} cm^2 s^{-1} along with the voltage. The lithium storage mechanism indicates that $Li_3V(MoO_4)_3$ can be considered a pre-lithiated material. In-situ XRD testing during the first cycle reflects the conversion reaction of $Li_3V(MoO_4)_3$. These insights will benefit the discovery of novel anode materials for lithium-ion batteries.

1. Introduction

The growing demand for renewable energy storage devices has generated mainstream interest in lithium-ion batteries (LIBs) for their high energy and power densities [1–4]. As one of the crucial components, anode material plays an important role in LIBs' performance [5–9]. Among the various anode materials, graphite is one of the most common in commercial applications [10,11]. However, the graphite's limited theoretical capacity (372 mAh g^{-1}) has proven too low to satisfy the increasing energy requirement [12–15]. Due to their high capacity, low cost and facile preparation, conversion-type transition metal oxides (TMOs) have been widely investigated as promising anodes [16–23]. However, these materials suffer from structural instability and low coulombic efficiency during the first cycle due to a large volume change, irreversible electrolyte decomposition and solid electrolyte interface (SEI) film formation [24,25]. In addition, TMO's high operating voltage makes it hard to significantly increase the energy density of batteries composed of TMO anodes [26,27]. Therefore, it is of great significance to develop new anode materials with large specific capacity, low operating voltage and improved initial coulombic efficiency (ICE).

Complex lithium- and molybdenum-containing oxides, such as $Li_2Co_2(MoO_4)_3$ [28], $Li_2Ni_2(MoO_4)_3$ [29], $LiFe(MoO_4)_2$ [30], $Li_3V(MoO_4)_3$[31] and $LiVO_2MoO_4$[32] have exhibited reversible Li^+ insertion/extraction over a wide voltage range. Among these materials, lithium vanadium molybdate, $Li_3V(MoO_4)_3$, was first proposed by the D. Mikhailova group in 2010 as a novel mixed molybdenum-vanadium oxide with an orthorhombic structure and large channels half-filled with Li atoms [31]. The Li^+ insertion/extraction ability of $Li_3V(MoO_4)_3$ was discovered in the potential window of 1.4–4.9 V, delivering a specific capacity of ~120 mAh g^{-1}. Interestingly, given the various oxidation states of V and Mo, it is expected that $Li_3V(MoO_4)_3$ has the ability to deliver a high specific capacity. Therefore, it is worth finding an effective way to develop the lithium storage ability of $Li_3V(MoO_4)_3$ under a suitable conditions. Moreover, the particle size of the $Li_3V(MoO_4)_3$ reported in the above-mentioned literature is as large as

* Corresponding author at: Powder Metallurgy Research Institute, Central South University, 932, Lushan South Road, Changsha 410083, PR China.
** Corresponding authors.
E-mail addresses: wangjiexikeen@csu.edu.cn (J. Wang), kshih@hku.hk (K. Shih), mlq518@whut.edu.cn (L. Mai).
[1] J. Wang, G. Zhang and Z. Liu contributed equally to this work.

https://doi.org/10.1016/j.nanoen.2017.11.079
Received 28 September 2017; Received in revised form 26 November 2017; Accepted 30 November 2017
Available online 05 December 2017

several micrometers, inhibiting both Li^+ ion transfer and electronic conductivity. Considering this, grain refining might be very useful for improving the electrochemical performance of $Li_3V(MoO_4)_3$.

In this work, we are the first to present the synthesis of $Li_3V(MoO_4)_3$ particles via a facile method using the soft chemical route with mechanical activation assist, and further study its lithium storage properties at low voltage. The synthetic method is simple, with the broad adaptability to the Li, Mo and V sources. Herein, oxalic acid is used not only as a selective reductant that reduces vanadium from a high oxidation state to V (+3) without reducing Mo(+6), but also as a carbon source depositing homogeneously on the surface of the $Li_3V(MoO_4)_3$ particles [4,33,34]. The residual carbon is able to enhance the electronic conductivity of the sample. With the assistance of mechanical activation, the as-prepared $Li_3V(MoO_4)_3$ particles are well-refined to submicron or nanoscale, which is beneficial to the lithium ion diffusion [35–37]. To explore the use of $Li_3V(MoO_4)_3$ in LIBs, the prepared $Li_3V(MoO_4)_3$ material is introduced as an anode material at the potential window ranging from 0.01 to 3.0 V. We expect to excavate the lithium ion storage properties of $Li_3V(MoO_4)_3$ at a low potential for practical application.

2. Experimental section

2.1. Synthesis of $Li_3V(MoO_4)_3$ material

The $Li_3V(MoO_4)_3$ material was prepared through a soft chemical route with mechanical activation assist followed by low temperature annealing. First, stoichiometric amounts of V_2O_5 (A.R., 99%) $CH_3COOLi{\cdot}2H_2O$ (A.R., 98%), $(NH_4)_6Mo_7O_{24}{\cdot}4H_2O$ (A.R., 99%) and 10% excess oxalic acid ($H_2C_2O_4{\cdot}2H_2O$, A.R., 99.5%) were mixed and dispersed into alcohol to form a homogeneous slurry. After that, the slurry was treated by high energy ball milling (ND6–2 L, 0.75 kW) for 8 h with a revolving speed of 200 r min^{-1}. Then, the obtained slurry was dried in the vacuum oven at 120 °C overnight. Finally, the precursor was sintered at 300 °C for 3 h, and then at 480 °C for 10 h in a tube furnace under an argon atmosphere to obtain $Li_3V(MoO_4)_3$.

2.2. Characterization of $Li_3V(MoO_4)_3$

Powder X-ray diffraction (XRD, Rint-2000, Rigaku, Cu Kα) was used to determine the purity and crystalline phases of the synthesized products. Field emission scanning electron microscope (FESEM, Hitachi S4800, 20 kV) and transmission electron microscopy (TEM, Titan G2 60–300 with image corrector) were used to observe the morphologies. The surface elemental valence states were determined by an X-ray photoelectron spectrometer (XPS, Kratos Model XSAM800) equipped with an Mg Kα achromatic X-ray source (1235.6 eV). The elemental distributions were evaluated by energy dispersive spectrometer (EDS) mapping analysis. The carbon content in the composite was determined by C-S analyzer (Eltar, Germany). For in-situ XRD measurement, an electrochemical cell module with a beryllium window directly cast with slurry was used. The XRD patterns of the cell at various discharge–charge states were then collected by a D8 Advance X-ray diffractometer using Cu-Kα radiation (λ = 1.5418 Å).

2.3. Electrochemical tests

To fabricate the working electrodes, 10% conductive agent (acetylene black), 10% binder (polyvinylidene fluoride) and 80% as-prepared active material were mixed into the N-methyl pyrrolidinone (NMP) solution to form slurry. Then, the resultant slurry was pasted on a copper foil current collector and dried at 120 °C for 6 h in a vacuum oven. Electrodes were punched into 12-mm-diameter disks. The quality of active material in each electrode was about 1.5 mg. The coin 2025 half cells were assembled in a dry Ar-filled glove box using $Li_3V(MoO_4)_3$ as a working electrode, lithium foil as a counter electrode and a porous polypropylene film as the separator. The electrolyte was a mixture solvent of 1 mol L^{-1} $LiPF_6$ in EC/EMC/DMC (1:1:1 in volume). The electrochemical tests were conducted using a NEWARE battery circler, between 0.01 V and 3.0 vs. Li^+/Li at room temperature. When calculating the specific capacity, the prepared sample with carbon layer directly amounted to the total mass of active material. A CHI660A electrochemical analyzer was used to conduct the electrochemical impedance spectroscopy and cyclic voltammetry measurements. A CV test was conducted in a voltage range of 0.01–3.0 V vs. Li^+/Li electrode at a scanning rate of 0.05 mV s^{-1}. The impedance spectra were recorded by applying an AC voltage of 5 mV amplitude in the 0.01 Hz–100 kHz frequency range. For the galvanostatic intermittent titration technique (GITT) measurement, the cell (pre-activated for 2 cycles) was discharged/charged with a constant current flux (100 mA g^{-1}) for 10 min followed by an open-circuit stand for 100 min.

3. Results and discussion

3.1. Structure and morphology

The structural characterization of the as-prepared $Li_3V(MoO_4)_3$ anode material was conducted using X-ray diffraction. The XRD pattern and Bragg peak position of the synthesized $Li_3V(MoO_4)_3$ are shown in Fig. 1(a). The XRD data are refined with Fullprof. According to the fitting results, as-prepared $Li_3V(MoO_4)_3$ is isostructural to

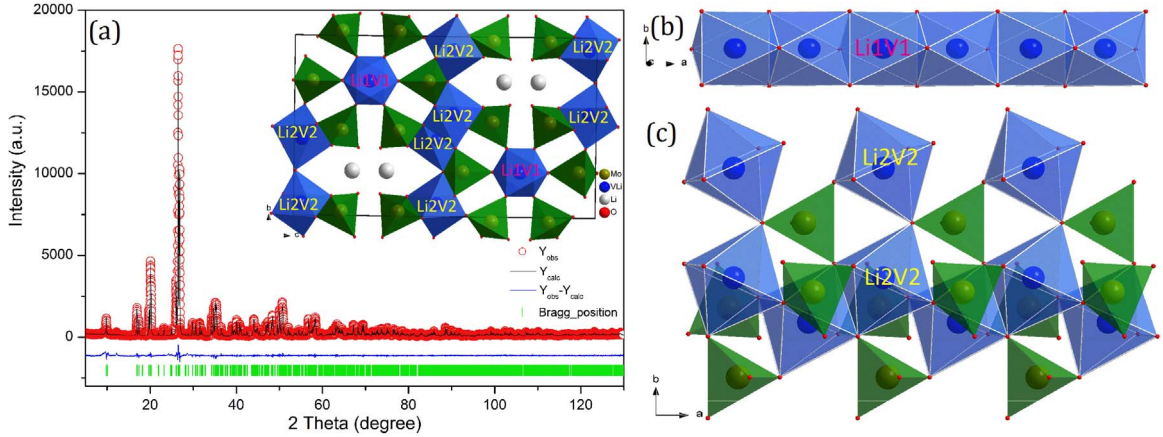

Fig. 1. (a) Refinement for powder XRD pattern of as-prepared $Li_3V(MoO_4)_3$; Inset is the crystal structure originated from the refinement. (b) Local crystal structure illustration of $[Li_{0.558}V_{0.442}]_{4c}O_6$ showing face sharing paralleling to b-c plane. (c) Local crystal structure illustration of $[Li_{0.652}V_{0.348}]_{8d}O_6$ at the a-b plane.

Table 1
Refined structural and positional parameters of as-prepared $Li_3V(MoO_4)_3$.

Space group: *Pnma*–orthorhombic
a = 5.07755(1) Å; b = 10.46078(2) Å; c = 17.54015(4) Å; cell volume = 931.65(6) Å^3

Atom	Site	*X*	*y*	*z*	Occ.
Mo(1)	4*c*	0.22034(6)	−0.25	0.05754(1)	1.000
Mo(2)	8*d*	0.27893(4)	−0.02594(1)	−0.15591(1)	1.000
V(1)	4*c*	0.61100(22)	0.25	−0.24833(7)	0.442
Li(1)	4*c*	0.61100(22)	0.25	−0.24833(7)	0.558
V(2)	8*d*	0.75064(24)	−0.07250(8)	−0.02536(5)	0.348
Li(2)	8*d*	0.75064(24)	−0.07250(8)	−0.02536(5)	0.652
Li(3)	4*c*	0.79095(119)	−0.25	−0.19313(29)	1.000
O(1)	8*d*	0.35884(26)	0.11776(13)	−0.20292(9)	1.000
O(2)	8*d*	0.07925(34)	−0.12250(12)	−0.21349(9)	1.000
O(3)	8*d*	0.55211(29)	−0.10977(13)	−0.12438(8)	1.000
O(4)	8*d*	0.42151(29)	−0.11762(12)	0.03421(9)	1.000
O(5)	4*c*	0.14201(34)	−0.25	0.15781(11)	1.000
O(6)	8*d*	0.08365(29)	0.00813(14)	−0.07317(9)	1.000
O(7)	4*c*	−0.05825(39)	−0.25	−0.00537(12)	1.000

orthorhombic (*Pnma* space group) NASICON-type $NaCo_{2.31}(MoO_4)_3$ [30,38]. In $Li_3V(MoO_4)_3$ structure, there are many cation vacancies which is good for the transmission of Li^+ ions [39]. No impurity phase is detected and a pure $Li_3V(MoO_4)_3$ phase can be synthesized using the current approach. As shown in [Fig. S1], the high-resolution V 2p spectrum shows two peaks with binding energies at 517.0 (V $2p_{3/2}$) and 524.3 eV (V $2p_{1/2}$), indicating the formation of V(+3) during synthetic process. While in Mo 3d spectrum, two obvious signals at 232.7 and 235.9 eV are separately attributed to the Mo $3d_{5/2}$ and Mo $3d_{3/2}$ of Mo^{6+}, which is in good agreement with previous reports [40]. These XPS results further reflect the successful fabrication of $Li_3V(MoO_4)_3$ with the expected valence state. In Table 1, the refined lattice parameters are a = 5.07755(1), b = 10.46078(2) and c = 17.54015(4), which are a little larger than those in the previous report. The enlarged cell parameters may benefit lithium ion diffusion and storage. From the structural view, the composition of the as-prepared sample can be described as $Li[Li_{0.558}V_{0.442}][Li_{0.652}V_{0.348}]_2[MoO_4]_3$. As shown in the inset of Fig. 1(a), two types of (Li, V) octahedral are found in the structure. One is face-sharing $[Li_{0.558}V_{0.442}]_{4c}O_6$ in the b-c plane [Fig. 1(b)]; the other is edge- and corn er-sharing $[Li_{0.652}V_{0.348}]_{8d}O_6$ that are linked with MoO_4 tetrahedra by vertices sharing [Fig. 1(c)]. Both $[Li_{0.558}V_{0.442}]_{4c}O_6$ and $[Li_{0.652}V_{0.348}]_{8d}O_6$ are linked with MoO_4 tetrahedra by sharing vertices. Similar to the structure of $Mg_{2.5}VMoO_8$ and $Cu_3Fe_4(VO_4)_6$, the Li_{4c} atoms in the $Li_3V(MoO_4)_3$ occupy the channel with a half-filled state. Part of the lithium positions are vacant along the infinite chain of face sharing octahedra, and the lithium atoms likely alternate with cation vacancies along the chain. As revealed by Table S1, the Li-O bond length of LiO_6 in the half-filled channel is larger than that in (Li, V)O_6, indicating easier transport for Li^+ in the channel.

Fig. 2 presents the morphologies of the $Li_3V(MoO_4)_3$ sample using SEM and TEM. The SEM images in Fig. 2(a) and (b) show the agglomerations of primary submicron-sized $Li_3V(MoO_4)_3$ particles with clean, smooth surfaces. The particle size of the as-prepared $Li_3V(MoO_4)_3$ exhibits a narrow distribution ranging from 200 to 400 nm. In addition, the agglomeration of the primary particles builds a porous structure in the prepared sample that is beneficial to the electrical contact between the electrode material and electrolyte. As a result, the lithium ion diffusion is enhanced by shortened transportation [5,27,41]. From the TEM and HRTEM images of $Li_3V(MoO_4)_3$ in Fig. 2(c) and (d), it can be seen that the surfaces of the well-crystallized $Li_3V(MoO_4)_3$ particles are wrapped loosely by a 5-nm pyrolytic amorphous carbon layer, forming a core/shell structure with an integral and uniform carbon shell. The content of carbon in the composite is about 0.95%. The FFT image of the selected area “1” [bottom right of Fig. 2(d)] and the corresponding IFFT image [Fig. 2(e)] show a lattice

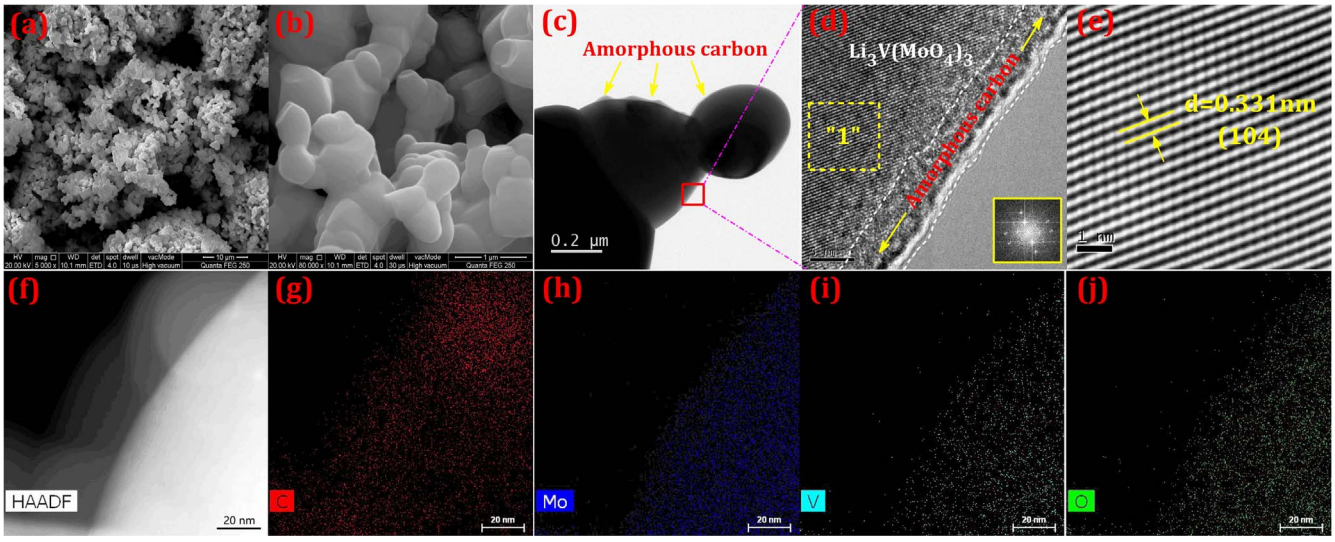

Fig. 2. Morphologies and microstructures of as-prepared $Li_3V(MoO_4)_3$: (a, b) SEM images of as-prepared $Li_3V(MoO_4)_3$ in different amplifications showing uniform submicron particles; (c) typical TEM and (d) high-resolution TEM (HRTEM) images of $Li_3V(MoO_4)_3$ sample showing the boundary of amorphous carbon shell and $Li_3V(MoO_4)_3$ crystal core; (e) IFFT image of $Li_3V(MoO_4)_3$ lattice showing (104) lattice plane; (f-j) EDS mappings showing the distribution of (g) C, (h) Mo, (i) V and (j) O.

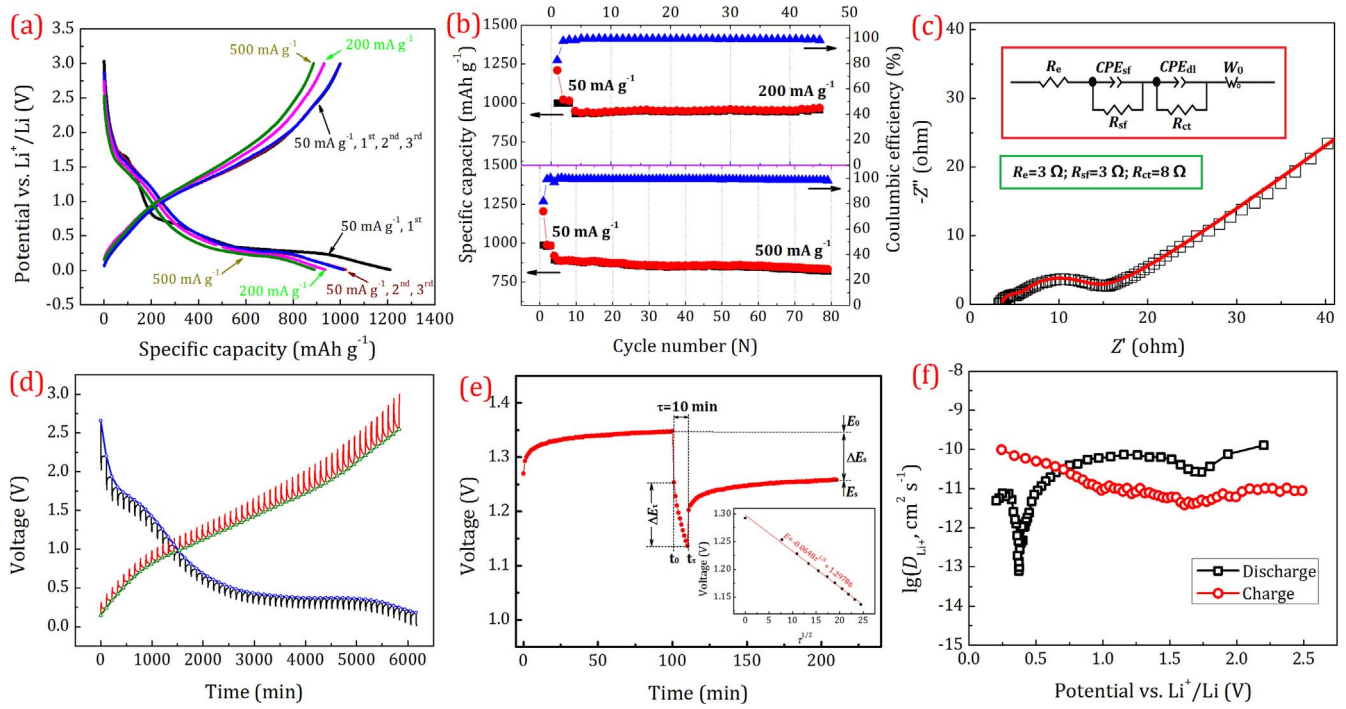

Fig. 3. (a) Selected galvanostatic charge-discharge curves in the potential range of 0.01–3.0 V at 50, 200 and 500 mA g^{-1}; (b) Profiles of specific capacity vs. cycle number at 200 and 500 mAh g^{-1}; (c) Nyquist plot of as-prepared $Li_3V(MoO_4)_3$ obtained after two cycles under open circuit voltage; Inset is the equivalent circuit diagram used to fit the as-obtained Nyquist plot. (d) GITT curves of $Li_3V(MoO_4)_3$ anode as a function of time in the voltage range of 3–0.01 V during both discharge and charge processes; The condition is controlled by repeatedly applying 100 mA g^{-1} for 10 min followed by an open-circuit stand for 100 min; (e) Scheme for a single titration step of GITT curves; Inset is the linear fit of the cell voltage (E) as a function of the square root of time ($\tau^{1/2}$); (f) D_{Li+} values in the $Li_3V(MoO_4)_3$ anode as a function of open-circuit voltage.

distance of 0.331 nm, corresponding to the (104) plane of the $Li_3V(MoO_4)_3$. The elemental EDS mappings in Fig. 2(f-j) further confirm that the bulk core material (as shown in Fig. 2(f)) is the $Li_3V(MoO_4)_3$ crystal with homogeneous elemental (V, Mo, O) distribution and that the surfaces of $Li_3V(MoO_4)_3$ particles are surrounded by carbon film. The carbon is derived from the extra oxalic acid, and may improve the electronic conductivity of $Li_3V(MoO_4)_3$ [42–45]. As a result, the carbon-coated $Li_3V(MoO_4)_3$ exhibits good electrochemical performance.

3.2. Electrochemical performance

The electrochemical performance of $Li_3V(MoO_4)_3$ as an anode material was investigated in the potential range of 0.01–3.0 V vs. Li^+/Li at room temperature. Fig. 3(a) presents the galvanostatic charge–discharge profiles of $Li_3V(MoO_4)_3$ at 50, 200 and 500 mA g^{-1}. The first discharge cycling curve exhibits a working lithiation plateau at about 1.65 V, which is related to the reaction of V(+3) to V(+2) during the cycling process. The capacity at this plateau is about 100 mAh g^{-1}. Encouragingly, there are long plateaus at around 0.6 and 0.3 V, which can be assigned to a typical conversion-reaction-based lithium storage accompanied with Faradic capacitance. This phenomenon is very common in most metal oxides with very high capacity [46]. This extraordinary discovery indicates that $Li_3V(MoO_4)_3$ can be used as a promising anode material at low voltage. As a result, at a current density of 50 mA g^{-1}, the $Li_3V(MoO_4)_3$ electrode delivers initial discharge and charge capacities of 1210 and 999 mAh g^{-1}, respectively. Remarkably, it possesses a high ICE of 82.6%. As the charge cut-off potential is decreased, the ICE and capacity decreased (Fig. S2). As shown in Table 2, $Li_3V(MoO_4)_3$ delivers an encouraging capacity as high as nano-TMOs. However, the ICE of $Li_3V(MoO_4)_3$ is much larger than that of TMOs. Moreover, the operating voltage of $Li_3V(MoO_4)_3$ is lower than that of TMOs. All of these characteristics make $Li_3V(MoO_4)_3$ a more promising anode material for LIBs with higher efficiency, better matching capability and larger energy density compared with TMOs.

Table 2
Comparison on capacity, initial coulombic efficiency, and average charging voltage (the voltage of half charging capacity) of typical TMOs and as-prepared $Li_3V(MoO_4)_3$.

Materials	Specific capacity (mAh g^{-1})/ current density (mA g^{-1})	Initial coulombic efficiency (%)	Average charging voltage (V)	Reference
Co_3O_4	950/50	76.2	2.0	[51]
NiO	700/156	70.6	1.9	[52]
CuO	650/100	61.5	1.95	[53]
$ZnCo_2O_4$	1104/100	71.5	1.7	[25]
$CoMoO_4$	1035/100	76.4	1.6	[54]
MoO_3	1123/223	48.0	1.6	[55]
Ni-Co oxides	1194/200	54.9	1.9	[17]
$NiCo_2O_4$	855/100	65.7	1.8	[18]
Co_2VO_4	1030/1000	–	1.85	[56]
$Li_3V(MoO_4)_3$	999/50	82.6	1.4	This work

After the first cycle, the curves in the following cycles overlap, indicating good cycle repeatability for the $Li_3V(MoO_4)_3$ electrode. The charge–discharge profiles at 200 and 500 mA g^{-1} maintain a similar shape as that at 50 mA g^{-1}, but exhibit some potential polarization and capacity fading. In particular, the reversible capacities of $Li_3V(MoO_4)_3$ are 931 and 890 mAh g^{-1} at 200 and 500 mA g^{-1}, respectively. In Fig. 3(b), it can be seen that the $Li_3V(MoO_4)_3$ electrode shows good cycle performance, with ~100% and 92.0% of capacity retention after 40 and 75 cycles at 200 and 500 mA g^{-1}, respectively. As presented in Fig. S3, $Li_3V(MoO_4)_3$ can deliver a reversible capacity of ~350 mAh g^{-1} even under the high current density of 1600 mA g^{-1}, which is higher than that of the commercial graphite anode. In addition, the electrochemical performance of $Li_3V(MoO_4)_3$ is expected to be further improved by appropriate approaches such as structural optimization and conductive agent modification. Fig. 3(c) shows the Nyquist plot of the $Li_3V(MoO_4)_3$ electrode at 3.0 V after cycling 2 times; specifically, two semi-circles in the high-to-medium frequency region and a straight

line in the low-frequency region. The intercept at the Z' axis in the high frequency refers to the ohmic resistance of the cell (R_e), and the value of R_e is only several ohms. One semicircle at high frequency corresponds to surface film impedance ($R_{sf}//CPE_{sf}$) and the other at middle frequency is indexed with charge transfer impedance ($R_{ct}//CPE_{dl}$). The sloping line in the low frequency region refers to the semi-infinite diffusion of lithium-ion (Warburg impedance, W_o). The impedance spectra are fitted by the equivalent electrical circuit as shown in the inset of Fig. 3(c). The values of R_{sf} and R_{ct} for $Li_3V(MoO_4)_3$ are only 3 and 8 Ω, respectively, indicating that $Li_3V(MoO_4)_3$ has a preeminent and stable interface that is beneficial for charge mobility and electrochemical reactions. This might be one reason why $Li_3V(MoO_4)_3$ exhibits good electrochemical performance as an anode material. It is well known that Li^+ diffusion within the compounds (D_{Li+}) is one of the factors affecting the kinetics of the electrochemical reaction in LIBs. Fig. 3(d) shows the GITT curves of $Li_3V(MoO_4)_3$ as a function of time. To obtain such continuous curves, the activated cell repeatedly experiences 100 mA g^{-1} for 10 min, followed by an open-circuit stand for 100 min Fig. 3(e) demonstrates a typical amplified single titration, schematically presenting the meanings of E_0, E_s, τ, $\triangle E_s$ and $\triangle E_\tau$. Assuming that the voltage can reach a new steady state at the end of each titration, the D_{Li+} can be determined by applying Fick's second law of diffusion and be calculated using the following equation (Eq. (1)) [47]:

$$D_{Li^+} = \frac{4}{\pi}\left(\frac{m_B V_M}{M_B A}\right)^2\left(\frac{\Delta E_s}{\tau(dE_\tau/d\sqrt{\tau})}\right)^2\left(\tau \ll \frac{L^2}{D_{Li^+}}\right) \quad (1)$$

where M_B, V_M and m_B are the molecular weight, molar volume and mass of the material, respectively. Given the liner relationship between E and $\tau^{1/2}$ [Inset of Fig. 3(e)], Eq. (1) can be simplified as:

$$D_{Li^+} = \frac{4}{\pi\tau}\left(\frac{m_B V_M}{M_B A}\right)^2\left(\frac{\Delta E_s}{\Delta E_\tau}\right)^2 \quad (2)$$

Based on Eq. (2), the calculated D_{Li+} as a function of voltage is shown in Fig. 3(f). It can be seen that the D_{Li+} values range from 10^{-10} to 10^{-13} cm^2 s^{-1} during discharging and from 10^{-10} to 5×10^{-12} cm^2 s^{-1} during charging. Overall, the D_{Li+} values present a decreasing trend during both discharging (from 3 to 0.01 V) and charging (from 0.01 to 3 V). During most of the voltage range, the D_{Li+} values show only a little difference (10^{-10}~10^{-11} cm^2 s^{-1}). However, the D_{Li+} values decrease rapidly near the end of the discharge process, indicating largely increased Li^+ diffusion resistance due to high Li^+ concentration in $Li_3V(MoO_4)_3$ at the end of discharging. Notably, calculated D_{Li+} values of $Li_3V(MoO_4)_3$ exhibit levels similar to those of the $Li_3V_2(PO_4)_3$ and $LiVPO_4F$ anodes [48,49], which are more preponderant compared to that of nano-Si [50]. As such, $Li_3V(MoO_4)_3$ can also be used as a promising anode material with good lithium ion mobility.

3.3. Lithium storage mechanism and in-situ XRD measurement

The CV curves of the $Li_3V(MoO_4)_3$ electrode for the first three cycles are presented in Fig. 4(a). In the first negative scan, the $Li_3V(MoO_4)_3$ electrode displays an intensive peak located at around 1.615 V (R_{11}), which is associated with the insertion of Li^+ into the channel of $Li_{3+x}V(MoO_4)_3$ [Eq. (3)] due to its half-filled characteristic. This phenomenon can also be observed in another lithium-containing metal molybdate, $LiFe(MoO_4)_2$ [30]. After that, the subsequent peaks at around 0.49 (R_{12}) and 0.12 V (R_{13}) correspond to the conversion of Mo(+6) to Mo(0) and V(+3) to V(0) [Eq. (4)], accompanied by the decomposition of the electrolyte and formation of SEI film [57]. During the first positive scan, the O_{11} peak located at 1.29 V is indexed with the transformation of metallic Mo to MoO_2 [Eq. (5)]; the broad O_{12} peak located at 1.79 V reflects the overlap of the conversions of MoO_2 to MoO_3 [Eq. (6)] and V to V_2O_3 [Eq. (7)] [54,58–61]. The O_3 peak at 2.38 V is associated with the oxidation of V_2O_3 to VO_2 [Eq. (8)]. [The XPS spectrum after one cycle in Fig. S4 indicates the high oxidative state (+4) of V]. After the first cycle, the cathodic R_{21}, R_{22} peaks are the reflection of lithium inserting into Li_mVO_2 [Eq. (9)] and Li_nMoO_3[Eq. (10)], respectively; R_{23}, R_{24} peaks correspond to the reduction of Li_mVO_2 and Li_nMoO_3 to metallic V [Eq. (11)]and Mo [Eq. (12)], respectively. Note that, during the first cycle, the electrode stores 21 mol Li^+ and releases 22 mol Li^+ per mol $Li_3V(MoO_4)_3$. As a result, the $Li_3V(MoO_4)_3$ can be regarded as a "pre-lithiated" anode material and its initial coulombic efficiency may be higher than traditional TMOs [Table 2]. In addition, the CV curves after the first cycle overlap, indicating good reversibility and repeatability during cycling. In-situ XRD characterization [Fig. 4(b, c, d)] is conducted to better understand the reaction mechanism and structural change of $Li_3V(MoO_4)_3$ during the first cycle. Fig. 4(b) and (d) show the three-dimensional in-situ XRD pattern of intensity and selected diffraction peaks of (122), (104), (026) and (200) for $Li_3V(MoO_4)_3$ during cycling. In the first discharging, above 0.55 V, the peaks almost maintain the principle intensity and peak (104) merges into peak (122). After that, the characteristic peaks for $Li_3V(MoO_4)_3$ decrease gradually and finally disappear at the end of the last plateau (~0.25 V). This indicates that during the first discharging, the initial structure of $Li_3V(MoO_4)_3$ is damaged and an amorphous phase is formed. In this state, the amorphous Mo^0 will be rearranged and leading to many lattice defects in structure, which is benefit for the transfer of lithium ions [62,63]. When recharging to 3.0 V, there is still no peak observed in the XRD curves, indicating that the subsequent lithium storage reaction occurs in the amorphous material without re-crystallization. It is a typical reflection of the conversion-type of $Li_3V(MoO_4)_3$ during the first cycling [30,60]. As shown in Fig. S5, after the first cycle, the material presents both amorphous and crystal phases. Moreover, many nano crystals are homogenously distributed in the amorphous media. These results prove the structural recombination of the $Li_3V(MoO_4)_3$ during the first cycling.

$$Li_3V(MoO_4)_3 + xLi^+ + xe^- -> Li_{3+x}V(MoO_4)_3 (x \le 1) \quad (3)$$

$$Li_{3+x}V(MoO_4)_3 + (21\text{-}x)Li^+ + (21\text{-}x)e^- -> V^0 + 3Mo^0 + 11Li_2O \quad (4)$$

$$Mo^0 + 2Li_2O <-> MoO_2 + 4Li^+ + 4e^- \quad (5)$$

$$MoO_2 + Li_2O <-> MoO_3 + 2Li^+ + 2e^- \quad (6)$$

$$2V^0 + 3Li_2O <-> V_2O_3 + 6Li^+ + 6e^- \quad (7)$$

$$V_2O_3 + Li_2O <-> 2VO_2 + 2Li^+ + 2e^- \quad (8)$$

$$VO_2 + mLi^+ + 2e^- <-> Li_mVO_2 + Li_2O (m \le 2) \quad (9)$$

$$MoO_3 + nLi^+ + ye^- <-> Li_nMoO_3 (n \le 2) \quad (10)$$

$$Li_mVO_2 + (4\text{-}m)Li^+ + (4\text{-}m)e^- <-> V^0 + 2Li_2O \quad (11)$$

$$Li_nMoO_3 + (6\text{-}n)Li^+ + (6\text{-}n)e^- <-> Mo^0 + 3Li_2O \quad (12)$$

4. Conclusions

$Li_3V(MoO_4)_3$ was successfully prepared through the low-temperature sintering of the precursor obtained via the mechanically activated soft chemical method for the first time. Well-crystalline $Li_3V(MoO_4)_3$ submicron/nanoscale particles with homogenous carbon coating were obtained via this facile route. $Li_3V(MoO_4)_3$ was innovatively used as an anode material at the low potential of 3.0–0.01 V, and showed good electrochemical performance including high capacity, large coulombic efficiency and stable cycle performance. Moreover, this work presented the conversion reaction mechanism for the lithium storage of $Li_3V(MoO_4)_3$ and prelithiation characteristics of $Li_3V(MoO_4)_3$ at low voltage. Given the relatively high chemical diffusion coefficient of Li^+, the electrochemical performance of $Li_3V(MoO_4)_3$ could be further improved through structural optimization and conductive agent modification. This work reflects the potential of $Li_3V(MoO_4)_3$ as an anode

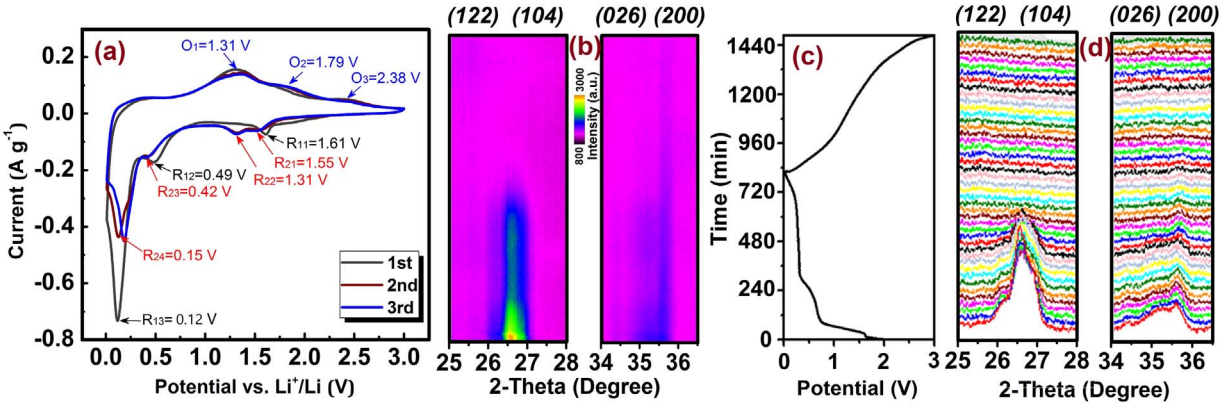

Fig. 4. (a) CV curves of as-fabricated $Li_3V(MoO_4)_3$ anode at the scanning rate of 0.05 mV s^{-1}; (b) the three-dimensional in-situ XRD pattern of intensity reflected by colors; (c) the initial galvanostatic charge–discharge profile of $Li_3V(MoO_4)_3$ during in-situ XRD analysis process; (d) the general changes in the selected diffraction peaks for $Li_3V(MoO_4)_3$.

for LIBs and opened up innovations in the design of novel, high-performance electrode materials for energy storage and conversion.

Acknowledgments

This work was supported by the National Natural Science Foundation of China (Grant No. 51704332, 51574287), the National Postdoctoral Program for Innovative Talents (BX201700290), and the T21-711/16R and 17212015 from the Research Grants Council (RGC) of the Government of Hong Kong SAR. We also thank the Advanced Research Center of CSU for performing the HRTEM examination.

Appendix A. Supporting information

Supplementary data associated with this article can be found in the online version at http://dx.doi.org/10.1016/j.nanoen.2017.11.079.

References

[1] S. Hy, H. Liu, M. Zhang, D. Qian, B.-J. Hwang, Y.S. Meng, Energy Environ. Sci. 9 (2016) 1931–1954.
[2] Q. Li, J. Sheng, Q. Wei, Q. An, X. Wei, P. Zhang, L. Mai, Nanoscale 6 (2014) 11072–11077.
[3] Q. Wei, S. Tan, X. Liu, M. Yan, F. Wang, Q. Li, Q. An, R. Sun, K. Zhao, H. Wu, L. Mai, Adv. Funct. Mater. 25 (2015) 1773–1779.
[4] J. Wang, Z. Liu, G. Yan, H. Li, W. Peng, X. Li, L. Song, K. Shih, J. Power Sources 329 (2016) 553–557.
[5] J. Wang, Q. Zhang, X. Li, B. Zhang, L. Mai, K. Zhang, Nano Energy 12 (2015) 437–446.
[6] H. Liu, W. Li, D. Shen, D. Zhao, G. Wang, J. Am. Chem. Soc. 137 (2015) 13161–13166.
[7] X. Li, J.-H. Cho, N. Li, Y. Zhang, D. Williams, S.A. Dayeh, S.T. Picraux, Adv. Energy Mater. 2 (2012) 87–93.
[8] M.N. Obrovac, V.L. Chevrier, Chem. Rev. 114 (2014) 11444–11502.
[9] Y. Chen, X. Li, X. Zhou, H. Yao, H. Huang, Y.-W. Mai, L. Zhou, Energy Environ. Sci. 7 (2014) 2689.
[10] Y.R. Cui, J.S. He, X.M. Li, J.X. Zhao, A.L. Chen, J. Yang, Adv. Mater. Res. 631–632 (2013) 306–309.
[11] N. Nitta, F. Wu, J.T. Lee, G. Yushin, Mater. Today 18 (2015) 252–264.
[12] F. Ding, W. Xu, D. Choi, W. Wang, X. Li, M.H. Engelhard, X. Chen, Z. Yang, J.-G. Zhang, J. Mater. Chem. 22 (2012) 12745.
[13] J. Ji, H. Ji, L.L. Zhang, X. Zhao, X. Bai, X. Fan, F. Zhang, R.S. Ruoff, Adv. Mater. 25 (2013) 4673–4677.
[14] J. Lai, H. Guo, Z. Wang, X. Li, X. Zhang, F. Wu, P. Yue, J. Alloy. Compd. 530 (2012) 30–35.
[15] F. Wu, X. Li, Z. Wang, H. Guo, Z. He, Q. Zhang, X. Xiong, P. Yue, J. Power Sources 202 (2012) 374–379.
[16] G. Ren, Y. Li, Z. Guo, G. Xiao, Y. Zhu, L. Dai, L. Jiang, Nano Res. 8 (2015) 3461–3471.
[17] J. Leng, Z. Wang, X. Li, H. Guo, H. Li, K. Shih, G. Yan, J. Wang, J. Mater. Chem. A 5 (2017) 14996–15001.
[18] T. Li, X. Li, Z. Wang, H. Guo, Y. Li, J. Mater. Chem. A 3 (2015) 11970–11975.
[19] Y. Zhang, W. Zhang, M. Li, Z. Yang, G. Chen, Q. Wang, J. Mater. Chem. A 1 (2013) 14368–14374.
[20] T. Li, X. Li, Z. Wang, H. Guo, H. Guo, J. Wang, J. Mater. Chem. A 5 (2017) 13469–13474.
[21] Z.-S. Wu, G. Zhou, L.-C. Yin, W. Ren, F. Li, H.-M. Cheng, Nano Energy 1 (2012) 107–131.
[22] M.V. Reddy, G.V. Subba Rao, B.V. Chowdari, Chem. Rev. 113 (2013) 5364–5457.
[23] L. Mai, X. Tian, X. Xu, L. Chang, L. Xu, Chem. Rev. 114 (2014) 11828–11862.
[24] Z. Yan, Q. Hu, G. Yan, H. Li, K. Shih, Z. Yang, X. Li, Z. Wang, J. Wang, Chem. Eng. J. 321 (2017) 495–501.
[25] Q. Zhang, J. Wang, J. Dong, F. Ding, X. Li, B. Zhang, S. Yang, K. Zhang, Nano Energy 13 (2015) 77–91.
[26] Y. Wen, Y. Zhu, A. Langrock, A. Manivannan, S.H. Ehrman, C. Wang, Small 9 (2013) 2810–2816.
[27] J. Wang, X. Li, Z. Wang, B. Huang, Z. Wang, H. Guo, J. Power Sources 251 (2014) 325–330.
[28] K.M. Begam, S. Selladurai, M.S. Michaelland, S.R.S. Prabaharan, Ionics 10 (2004) 77–83.
[29] K.M. Begam, S.R.S. Prabaharan, J. Power Sources 159 (2006) 319–322.
[30] N. Chen, Y. Yao, D. Wang, Y. Wei, X. Bie, C. Wang, G. Chen, F. Du, ACS Appl. Mater. Interfaces 6 (2014) 10661–10666.
[31] D. Mikhailova, A. Sarapulova, A. Voss, A. Thomas, S. Oswald, W. Gruner, D.M. Trots, N.N. Bramnik, H. Ehrenberg, Chem. Mater. 22 (2010) 3165–3173.
[32] N. Chen, C. Wang, F. Hu, X. Bie, Y. Wei, G. Chen, F. Du, ACS Appl. Mater. Interfaces 7 (2015) 16117–16123.
[33] J. Wang, Z. Wang, X. Li, H. Guo, X. Wu, X. Zhang, W. Xiao, Electrochim. Acta 87 (2013) 224–229.
[34] J. Wang, X. Li, Z. Wang, H. Guo, Y. Zhang, X. Xiong, Z. He, Electrochim. Acta 91 (2013) 75–81.
[35] A.K. Rai, J. Gim, L.T. Anh, J. Kim, Electrochim. Acta 100 (2013) 63–71.
[36] C. Lin, X. Fan, Y. Xin, F. Cheng, M.O. Lai, H. Zhou, L. Lu, J. Mater. Chem. A 2 (2014) 9982.
[37] W. Tang, X. Wang, Y. Hou, L. Li, H. Sun, Y. Zhu, Y. Bai, Y. Wu, K. Zhu, T. Ree, J. Power Sources 198 (2012) 308–311.
[38] J.A. Ibers, G. Smith, Acta Crystallogr. 17 (1964) 190–197.
[39] J.P. Smit, T.M. McDonald, K.R. Poeppelmeier, Solid State Sci. 10 (2008) 396–400.
[40] Z. Yin, Y. Xiao, X. Wang, W. Wang, D. Zhao, M. Cao, Nanoscale 8 (2016) 508–516.
[41] Z. Liu, W. Peng, Z. Xu, K. Shih, J. Wang, Z. Wang, X. Lv, J. Chen, X. Li, ChemSusChem 9 (2016) 2122–2128.
[42] C. Zhang, X. Peng, Z. Guo, C. Cai, Z. Chen, D. Wexler, S. Li, H. Liu, Carbon 50 (2012) 1897–1903.
[43] G.-N. Zhu, H.-J. Liu, J.-H. Zhuang, C.-X. Wang, Y.-G. Wang, Y.-Y. Xia, Energy Environ. Sci. 4 (2011) 4016.
[44] L. Yang, L. Liu, Y. Zhu, X. Wang, Y. Wu, J. Mater. Chem. 22 (2012) 13148.
[45] M.F. Hassan, Z.P. Guo, Z. Chen, H.K. Liu, J. Power Sources 195 (2010) 2372–2376.
[46] E. Yoo, J. Kim, E. Hosono, H.-S. Zhou, T. Kudo, I. Honma, Nano Lett. 8 (2008) 2277–2282.
[47] W. Weppner, R.A. Huggins, J. Electrochem. Soc. 124 (1977) 1569–1578.
[48] X.H. Rui, N. Yesibolati, S.R. Li, C.C. Yuan, C.H. Chen, Solid State Ion. 187 (2011) 58–63.
[49] J. Wang, X. Li, Z. Wang, H. Guo, B. Huang, Z. Wang, G. Yan, J. Solid State Electr. 19 (2015) 153–160.
[50] N. Ding, J. Xu, Y.X. Yao, G. Wegner, X. Fang, C.H. Chen, I. Lieberwirth, Solid State Ion. 180 (2009) 222–225.
[51] X. Yin, Z. Wang, J. Wang, G. Yan, X. Xiong, X. Li, H. Guo, Mater. Lett. 120 (2014) 73–75.
[52] X. Li, A. Dhanabalan, K. Bechtold, C. Wang, Electrochem. Commun. 12 (2010) 1222–1225.
[53] Q. Zhang, J. Wang, D. Xu, Z. Wang, X. Li, K. Zhang, J. Mater. Chem. A 2 (2014) 3865–3874.
[54] C.T. Cherian, M.V. Reddy, S.C. Haur, B.V. Chowdari, ACS Appl. Mater. Interfaces 5 (2013) 918–923.
[55] Z. Wang, S. Madhavi, X.W. Lou, J. Phys. Chem. C 116 (2012) 12508–12513.
[56] C. Zhu, Z. Liu, J. Wang, J. Pu, W. Wu, Q. Zhou, H. Zhang, Small 13 (2017) 1701260.
[57] Z. Yin, Y. Xiao, X. Wang, W. Wang, D. Zhao, M. Cao, Nanoscale 8 (2016) 508–516.
[58] N.N. Leyzerovich, K.G. Bramnik, T. Buhrmester, H. Ehrenberg, H. Fuess, J. Power

Sources 127 (2004) 76–84.
[59] R.S. Liu, C.Y. Wang, V.A. Drozd, S.F. Hu, H.S. Sheu, Electrochem. Solid-State Lett. 8 (2005) A650.
[60] M.A. Reddy, M.S. Kishore, V. Pralong, V. Caignaert, U.V. Varadaraju, B. Raveau, J. Power Sources 168 (2007) 509–512.
[61] Z. Ju, E. Zhang, Y. Zhao, Z. Xing, Q. Zhuang, Y. Qiang, Y. Qian, Small 11 (2015) 4753–4761.
[62] D. Kiriya, P. Lobaccaro, H.Y. Nyein, P. Taheri, M. Hettick, H. Shiraki, C.M. Sutter-Fella, P. Zhao, W. Gao, R. Maboudian, J.W. Ager, A. Javey, Nano Lett. 16 (2016) 4047–4053.
[63] J. Yang, K. Wang, J. Zhu, C. Zhang, T. Liu, ACS Appl. Mater. Interfaces 8 (2016) 31702–31708.

Jiexi Wang is an associate professor of metallurgy and material Chemistry at Central South University (CSU). He is the winner of the National Postdoctoral Program for Innovative Talents under the supervision of Prof. Yong Liu. He received his Ph.D. degree in Metallurgical Physical Chemistry from CSU in 2015. Then he joined into Prof. T.S. Zhao's group as a visiting scholar at Hong Kong University of Science and Technology. After that, he was a post-doctoral research associate in the laboratory of Prof. X.Y. Li and K. Shih at The University of Hong Kong. His research focuses on nonferrous-based materials and corresponding resources for clean energy storage, such as high-power/high-energy lithium ion batteries and supercapacitors. He has published about 80 SCI papers with more than 1600 citations (H-index = 26).

Guobin Zhang received his B.S. degree from Inner Mongolia University of Science & Technology in 2014 and he is currently working toward the Ph.D. Degree in Wuhan University of Technology. His current research focuses on in situ characterization.

Zhaomeng Liu received his B.S. and Master degrees at the school of Metallurgy and Environment from CSU in 2014 and 2017, respectively. He is currently a Ph.D. candidate in Hunan University under the supervision of Prof. Bingan Lu. His research focuses on advanced materials for new energy storage devices.

Hangkong Li received his B.E. (2011) and M.E. (2014) degrees in materials science from CSU. Currently, he is a PhD student under the supervision of Dr. Kaimin Shih in the Department of Civil Engineering at The University of Hong Kong. His research interests focus on the crystal structural determination via XRD technique, nanomaterials for batteries and energy-related applications.

Yong Liu is the Dean of Powder Metallurgy Research Institute and Full-Professor of Materials Science and Engineering at CSU. He is the winner of the National Natural Science Fund for Distinguished Young Scholars. He is the Editorial Board member of *Intermetallics* and *Materials Characterization*. He received his Ph.D. degree from CSU in 1999. He carried out postdoctoral research work at CSU. Then, he worked at Oak Ridge National Laboratory in USA. In 2008, he worked as Alexander von Humboldt Research Fellow at RWTH Aachen University in Germany. His research interests are powder metallurgical techniques for nanometals, alloys and gradient cemented carbide. He has published more than 200 SCI paper in material area.

Zhixing Wang received his Ph.D. in physical chemistry from Department of Physical Chemistry, Central South University of Technology in 1998. From September 2001 to September 2002, He worked as a visiting scholar in Department of Applied Chemistry, Tokyo Institute of Technology, Japan. He is now a professor in School of Metallurgy and Environment, CSU. His research interests focus mainly on electrochemical theory, cathode materials for batteries and supercapacitors.

Xinhai Li received his Ph.D. in physical chemistry from Central South University of Technology in 1990. Currently he is a Professor and Director of the Engineering Center for Advanced Materials for Energy Storage in School of Metallurgy and Environment, CSU. He is an expert in energy database of China. He mainly works on carbon materials, nonferrous materials for batteries and supercapacitors, design and application of energy storage and conversion systems, electrolyte for lithium ion batteries, and resource-to-material metallurgy.

Professor Kaimin Shih leads an Environmental Materials Research Group at the University of Hong Kong. His research interests are the fabrication and characterizations of novel materials for environmental and energy applications, particularly focusing on the mineral-water interfacial reactions. Examples of his work include the advanced ceramics for metal incorporations, catalysts and membranes for environmental treatments, electrode materials for batteries, and sorbent materials for pollutant removals. He has published more than 160 SCI journal articles, edited 2 books (relevant to X-ray diffraction technique and environmental materials), and is currently an associate editor of the "Waste Management".

Liqiang Mai is Chair Professor of Materials Science and Engineering at Wuhan University of Technology (WUT). He is Cheung Kong Scholar Chair Professor and the winner of the National Natural Science Fund for Distinguished Young Scholars. His current research interests focus on new nanomaterials for electrochemical energy storage and micro/nano energy devices. He received his Ph.D. degree from WUT in 2004. He carried out his postdoctoral research in the laboratory of Prof. Zhong-Lin Wang at Georgia Institute of Technology in 2006–2007 and worked as advanced research scholar in the laboratory of Prof. Charles M. Lieber at Harvard University in 2008–2011. He worked as advanced research scholar in the laboratory of Prof. Peidong Yang at University of California, Berkeley in 2017.